Journal of Nuclear Materials 402 (2010) 1–7

Contents lists available at ScienceDirect

Journal of Nuclear Materials

journal homepage: www.elsevier.com/locate/jnucmat

Impact deformation behaviour of Ti–6Al–4V alloy in the low-temperature regime

Woei-Shyan Lee [a,*], Tao-Hsing Chen [b], Sian-Cing Huang [a]

[a] Department of Mechanical Engineering, National Cheng Kung University, Tainan 701, Taiwan
[b] Center for Micro/Nano Science and Technology, National Cheng Kung University, Tainan 701, Taiwan

ARTICLE INFO

Article history:
Received 6 March 2009
Accepted 16 April 2010

ABSTRACT

The impact response of Ti–6Al–4V alloy is investigated using a compressive split-Hopkinson pressure bar at strain rates of $1.0 \times 10^3\ s^{-1}$, $3.0 \times 10^3\ s^{-1}$ and $4.3 \times 10^3\ s^{-1}$ and temperatures of −150 °C, 0 °C and 25 °C, respectively. It is shown that for a constant temperature, the flow stress, work hardening rate and strain rate sensitivity increase with increasing strain rate, while the activation volume decreases. Meanwhile, for a constant strain rate, the activation volume increases with increasing temperature, while the flow stress, work hardening rate and strain rate sensitivity decrease. Scanning electron microscopy (SEM) observations reveal that the fracture surfaces are characterised by a transgranular dimpled structure, indicating that Ti–6Al–4V alloy has excellent ductility. The density of the dimples increases with an increasing strain rate or increasing temperature. Transmission electron microscopy (TEM) observations show that the dislocation density increases with an increasing strain rate, but decreases with an increasing temperature. The linear correlation between the square root of the dislocation density and the true stress confirms the existence of a Bailey–Hirsch type relationship. Finally, the strengthening effect observed at higher strain rates and lower temperatures is attributed to a greater dislocation density.

1. Introduction

Ti–6Al–4V alloy has attracted considerable interest recently because of its high specific strength, extensive ductility and good corrosion resistance [1–3]. These properties render Ti–6Al–4V an ideal candidate for a wide variety of components in the aerospace, defense, bio-medical and nuclear industries. Regarding the nuclear engineering applications of titanium alloys such as Ti–6Al–4V, modern nuclear-powered submarines are commonly built with titanium hulls, allowing the vessel to operate at depths of as much as 6000 m [4]. Similarly, titanium alloys are used to fabricate the body of nuclear missiles designed to operate at high flight velocities and altitudes of 50,000 m or more [5,6]. In both cases, the titanium alloy structure is subjected to a high strain rate and a low (2 °C for submarines) or cryogenic (−150 °C for missiles) temperature. To ensure the mechanical integrity of Ti–6Al–4V components, it is therefore essential to develop a thorough understanding of the effects of impact loading and cryogenic temperature on the alloy's mechanical properties and microstructural evolution.

It is well known that the mechanical properties and failure characteristics of most engineering metals and alloys vary with the strain rate and temperature [7–13]. For example, the impact flow stress of 304L stainless steel increases with an increasing strain rate. Furthermore, a notable increase in the strain rate sensitivity occurs at strain rates greater than a critical value of approximately $10^3\ s^{-1}$ [8]. When predicting the dynamic failure characteristics of engineering materials, this marked increase in the strain rate sensitivity must be taken into account. However, the effects of temperature on the mechanical properties of the material must also be considered [14–17]. For example, most metals and alloys experience a significant increase in flow stress and a dramatic reduction in ductility as the temperature is reduced to the cryogenic range. This effect is even more pronounced when the component is loaded under high strain rate conditions.

From a microstructural viewpoint, the plastic deformation of an engineering material is directly related to the motion of dislocations within the microstructure. The evolution of the dislocation structure depends on both the original structure of the material and the applied strain rate and temperature [18,19]. Furthermore, it has been reported that dislocations within the crystal structure form loops, pile up at the grain boundaries, or arrange themselves in various types of cells [20,21]. These various dislocation arrangements act as obstacles to the motion of other dislocations, and therefore provide a hardening effect [22,23]. The effect of the dislocation density on the hardening behaviour can be described by the following Bailey–Hirsch type relation [24]:

$$\sigma = \sigma_0 + \alpha_1 b G \sqrt{\rho}, \tag{1}$$

where ρ is the dislocation density, G is the shear modulus, b is the magnitude of the Burgers vector, α_1 is a material constant related to the crystal and grain structure, and σ_0 is the initial yield stress of the material.

* Corresponding author. Tel.: +886 6 2757575x62174; fax: +886 6 2352973.
E-mail address: wslee@mail.ncku.edu.tw (W.-S. Lee).

0022-3115/$ - see front matter © 2010 Elsevier B.V. All rights reserved.
doi:10.1016/j.jnucmat.2010.04.013

Ti–6Al–4V alloy has a poor thermal conductivity (6.7 W/m K), and thus it is important to clarify the adiabatic shearing effect in order to prolong the service life of Ti–6Al–4V components and to prevent their catastrophic behaviour. Although the high-temperature deformation behaviour of Ti–6Al–4V alloy has been extensively examined over a wide range of strain rates [25–28], the effects of strain rate on the impact response, failure characteristics and microstructural evolution of Ti–6Al–4V alloy in the low-temperature regime are less clear. Consequently, the present study utilises a compressive split-Hopkinson pressure bar (SHPB) to examine the impact deformation behaviour of Ti–6Al–4V alloy under strain rates ranging from $1.0 \times 10^3\ s^{-1}$ to $4.3 \times 10^3\ s^{-1}$ and temperatures of −150 °C, 0 °C and 25 °C, respectively. The respective effects of the strain rate and temperature on the stress–strain characteristics of the impacted specimens are identified and discussed. The fracture surfaces are then analysed using scanning electron microscopy (SEM) in order to identify the dominant fracture mechanism. Finally, transmission electron microscopy (TEM) is employed to observe the microstructures of the deformed specimens in order to correlate the mechanical response of the Ti–6Al–4V alloy and its microstructural evolution.

2. Material and experimental procedure

The Ti–6Al–4V alloy used in this study was purchased from B&S Aircraft Alloys, USA in the form of a hot-rolled bar with a length of 200 mm and a diameter of 27 mm. According to the supplier's specification, the chemical composition of the Ti–6Al–4V alloy was as follows: 6.1%Al, 4.0%V, 0.21%Fe, 0.1%C, 0.03%N, 0.012%H, 0.15%O, and a balance of Ti. The bar was annealed at 750 °C for 2 h and was then air-cooled in order to reduce the residual stress and ensure a uniform microstructure. Specimens with a length of 7 ± 0.1 mm and a diameter of 7.2 mm were then machined from the bar and finished to a final diameter of 7 ± 0.1 mm using a centre-grinding process. Dynamic impact tests were then carried out using a compressive SHPB at strain rates of $1.0 \times 10^3\ s^{-1}$, $3.0 \times 10^3\ s^{-1}$ and $4.3 \times 10^3\ s^{-1}$ and temperatures of −150 °C, 0 °C and 25 °C.

Fig. 1 presents a schematic illustration of the experimental arrangement. In the impact tests, the cylindrical specimens were sandwiched between the incident pressure bar and the transmitter bar and the end of the incident bar was then impacted by the strike bar. The strike, incident and transmitter bars were all made from high-strength tool steel and had a diameter of 12.7 mm. In addition, the incident and transmitter bars were both 100 cm in length, while the strike bar had a length of 22 cm. The low testing temperatures of 0 °C and −150 °C were obtained by fitting a refrigeration system around the specimen. Liquid nitrogen and alcohol were added to the refrigeration system at the beginning of the experimental tests and were periodically replenished in order to maintain a constant fluid level. (Note that the full details of the experimental procedure and analytical technique used to evaluate the dynamic mechanical response of the impacted specimens are presented in [29], and are therefore omitted here.)

Following the impact tests, fracture analysis specimens were prepared using a standard metallographic technique and were examined using an FEI Quanta 400F scanning electron microscope with an operating voltage of 15 kV. TEM samples were prepared by cutting foils with a thickness of 350 μm from the Ti–6Al–4V specimens using a low speed cutting machine. Discs with a diameter of 3 mm were then punched from each foil and polished in a solution of 95% ethyl alcohol and 5% perchloric acid at a temperature of 25 °C using a twin-jet electro-polishing machine with an agitation voltage of 20 V. Finally, the microstructural characteristics of the various specimens were examined using a JEOL TEM-3010 transmission electron microscope with an accelerating voltage of 200 kV.

3. Results and discussion

3.1. True stress–strain curves and mechanical behaviour

Figs. 2a–c present the true stress–strain curves of Ti–6Al–4V alloy for strain rates of $1.0 \times 10^3\ s^{-1}$, $3.0 \times 10^3\ s^{-1}$ and $4.3 \times 10^3\ s^{-1}$ and temperatures of 25 °C, 0 °C and −150 °C, respectively. In Fig. 2a, it can be seen that the flow stress depends on both the strain and the strain rate. Specifically, for a constant strain, the flow stress increases rapidly with increasing strain rate, while for a constant strain rate, the flow stress increases gradually with increasing strain. Similar tendencies are observed in Fig. 2b and c for deformation temperatures of 0 °C and −150 °C, respectively. From inspection, it is found that for a fixed true strain of 0.3 and a strain rate of $4.3 \times 10^3\ s^{-1}$, the flow stress increases from 1260.9 MPa to 1428.4 MPa as the temperature is reduced from 25 °C to −150 °C. The results presented in Fig. 2a–c show that the strain rate governs not only the flow stress, but also the facture strain. Specifically, for a given temperature, the fracture strain increases with an increas-

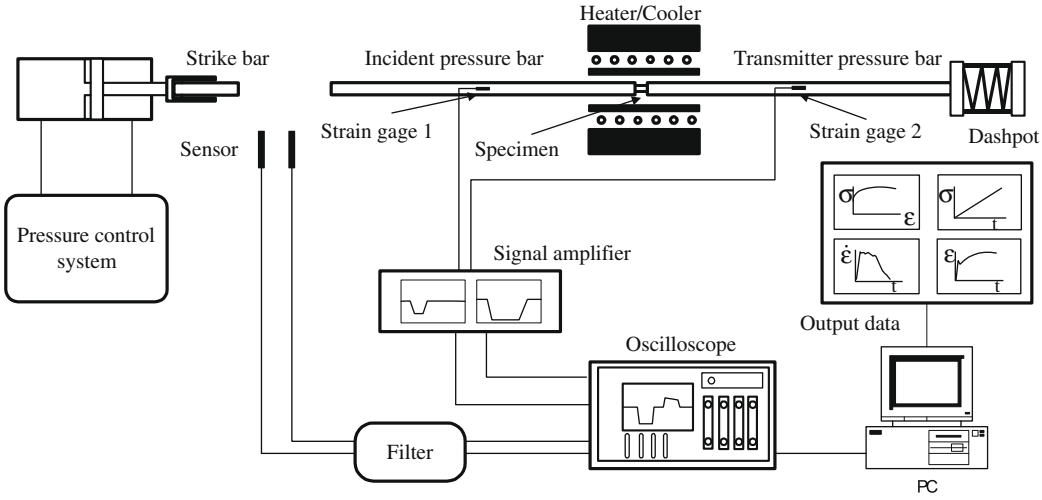

Fig. 1. Schematic illustration of compressive split-Hopkinson pressure bar with integrated refrigeration system.

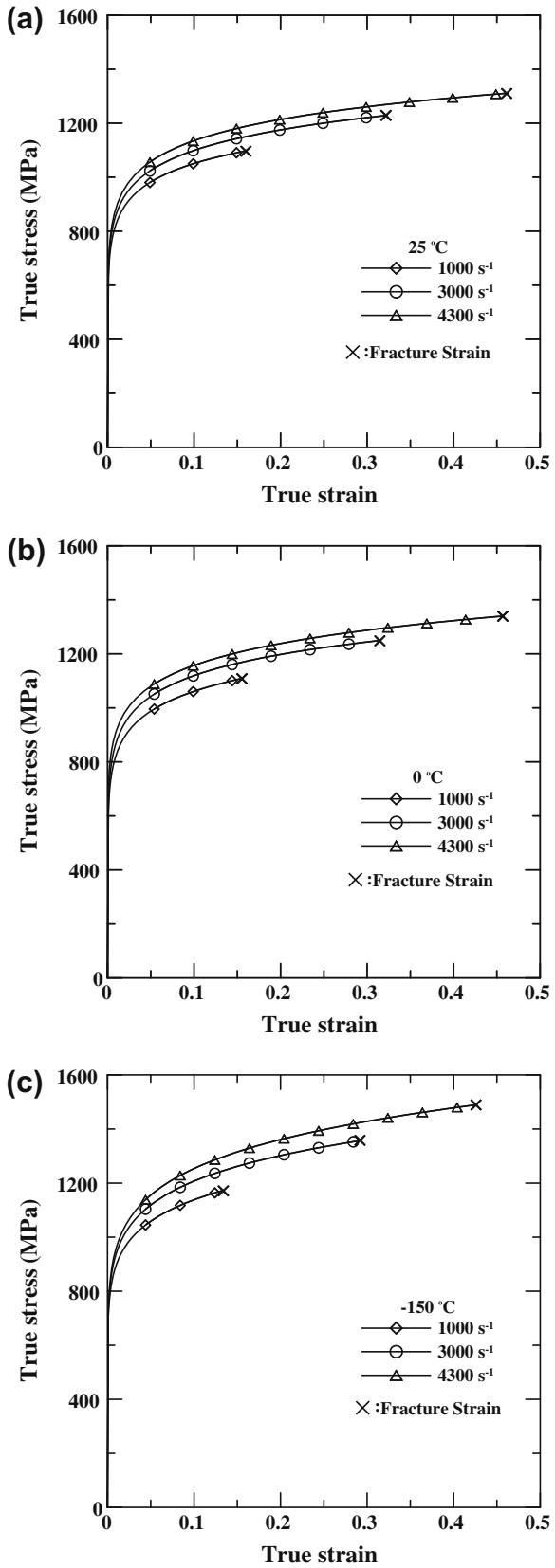

Fig. 2. True stress–strain curves of Ti–6Al–4V alloy deformed at strain rates of 1.0×10^3 s^{-1}, 3.0×10^3 s^{-1} and 4.3×10^3 s^{-1} and temperatures of (a) 25 °C, (b) 0 °C and (c) −150 °C, respectively.

ing strain rate. However, for a constant strain rate, the fracture strain reduces with a reducing temperature.

Table 1
Dynamic mechanical properties of Ti–6Al–4V alloy impacted at strain rates of 1.0×10^3–4.3×10^3 s^{-1} and temperatures of −150 °C, 0 °C and 25 °C.

T (°C)	Strain rate (s^{-1})	Yield strength A (MPa)	Material constants B (MPa)	Work hardening coefficient, n
−150	4300	876.58	973.72	0.4021
	3000	837.40	1000.96	0.3749
	1000	783.42	1038.92	0.3414
0	4300	784.13	816.57	0.3361
	3000	756.91	838.26	0.3183
	1000	721.18	866.46	0.2967
25	4300	751.91	819.94	0.3266
	3000	723.13	843.94	0.3091
	1000	685.17	875.22	0.2877

The flow stress relations shown in Fig. 2a–c can be described using the simple model proposed by Ludwik [30], i.e. $\sigma = A + B\varepsilon^n$, where A is the yield strength, B is a material constant, and n is the work hardening coefficient. Table 1 summarises the values of A, B and n for each of the strain rate/temperature conditions shown in Fig. 2a–c. The results show that the yield strength (A) and work hardening coefficient (n) increase with increasing strain rate at a fixed temperature, but decrease with increasing temperature for a given strain rate. This result suggests that a lower deformation temperature increases the density and multiplication rate of the dislocations within the Ti–6Al–4V microstructure, and prompts a corresponding improvement in the resistance of the alloy to plastic flow.

In Fig. 2a–c, the gradient of the stress–strain curves is equivalent to the work hardening rate ($d\sigma/d\varepsilon$). Therefore, for a given deformation temperature, it is evident that the work hardening rate of Ti–6Al–4V alloy is dependent on both the strain rate and the strain. Table 2 summarises the work hardening rate of the current Ti–6Al–4V alloy for each of the experimental conditions considered in Fig. 2a–c. It is observed that for a given temperature, the work hardening rate reduces with increasing strain for a constant strain rate, but increases with increasing strain rate at a constant strain. In addition, for a constant strain rate and strain, the work hardening rate reduces with an increasing temperature.

3.2. Strain rate sensitivity and activation volume

The stress–strain relations presented in Fig. 2a–c clearly show that the flow stress of Ti–6Al–4V alloy is significantly dependent on the strain rate. The strain rate sensitivity (β) of the Ti–6Al–4V alloy can be derived from the experimental results presented in Fig. 2a–c in accordance with the formulation [31]

$$\beta = (\partial\sigma/\partial \ln \dot{\varepsilon}) = \frac{\sigma_2 - \sigma_1}{\ln(\dot{\varepsilon}_2/\dot{\varepsilon}_1)}, \tag{2}$$

Table 2
Variation of work hardening rate of Ti–6Al–4V alloy at different strain rates and temperatures.

T (°C)	Strain rate (s^{-1})	Work hardening rate (MPa/unit strain)				
		$\varepsilon = 0.1$	$\varepsilon = 0.2$	$\varepsilon = 0.3$	$\varepsilon = 0.4$	$\varepsilon = 0.45$
−150	4300	1473.9	807.2	567.3	441.6	–
	3000	1313.2	708.5	–	–	–
	1000	1179.4	–	–	–	–
0	4300	1137.2	595.6	407.2	310.7	278.1
	3000	1114.7	566.9	380.4	–	–
	1000	1066.4	–	–	–	–
25	4300	1119.4	572.9	386.0	291.5	259.7
	3000	1062.1	539.7	360.3	–	–
	1000	985.8	–	–	–	–

where the flow stresses σ_2 and σ_1 are obtained in impact tests conducted at average strain rates of $\dot{\varepsilon}_2$ and $\dot{\varepsilon}_1$, respectively, and are calculated at the same value of plastic strain.

Fig. 3a plots the strain rate sensitivity of the Ti–6Al–4V alloy as a function of the true strain for two different strain rate ranges and temperatures of −150 °C, 0 °C and 25 °C, respectively. It can be seen that the strain rate sensitivity increases with increasing strain and strain rate, but decreases with increasing temperature.

Given the assumption that the plastic deformation of the current Ti–6Al–4V alloy is thermally-activated, the activation volume can be expressed in the following form [32]:

$$v^* = -\frac{\partial G^*}{\partial \sigma} = kT\left(\frac{\partial \ln \dot{\varepsilon}}{\partial \sigma}\right)_T, \tag{3}$$

where G^* is the activation energy, k is the Boltzmann constant, and T is the absolute temperature. Substituting the data presented in Fig. 2a–c into Eq. (3), the activation volume of Ti–6Al–4V alloy can be calculated and plotted as a function of the strain. The corresponding results are presented in Fig. 3b. Note that in compiling this figure, the activation volume is normalised by b^3, where b is the Burgers vector and has a value of 3.0×10^{-10} m for Ti–6Al–4V alloy

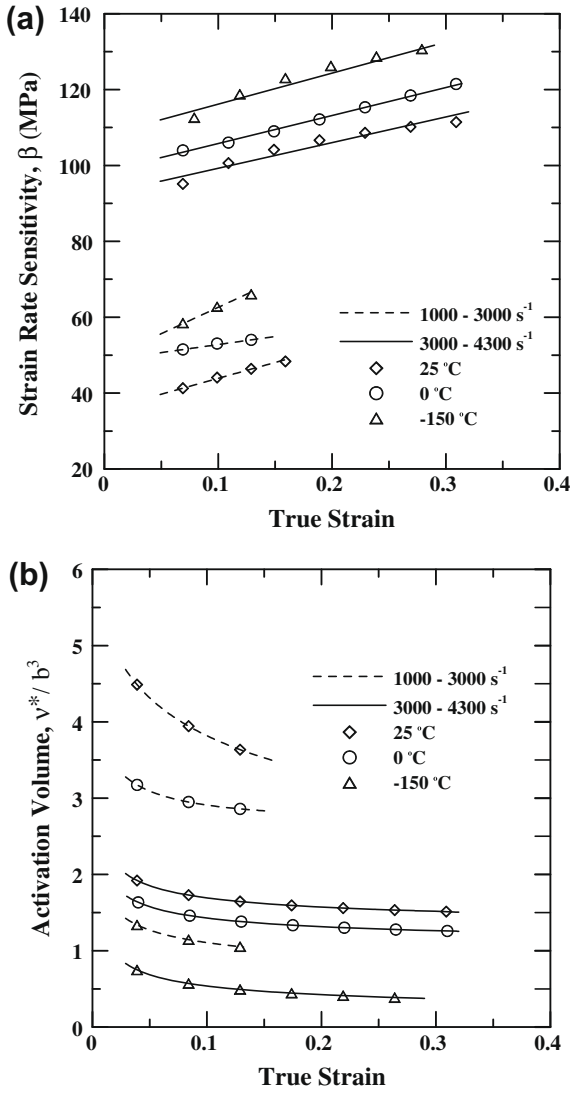

Fig. 3. (a) Variation of strain rate sensitivity of Ti–6Al–4V alloy with true strain as function of temperature and (b) variation of activation volume of Ti–6Al–4V alloy with true strain as function of temperature.

[33]. The results reveal that the activation volume increases with an increasing temperature at a fixed strain and strain rate, but decreases with an increasing strain rate at a constant temperature and strain. Finally, for a constant temperature and strain rate, the activation volume decreases with increasing true strain. From a general thermodynamic perspective, the thermal activation volume of a material helps dislocations in the microstructure overcome short-range barriers to movement. In the current study, the relatively low values of the activation energy imply that the dislocations in the Ti–6Al–4V microstructure require a higher driving force to overcome short-range obstacles when deformation takes place under high strain rate or low temperature conditions.

3.3. Fracture surface observations

Fig. 4 presents a low-magnification SEM fractograph of a specimen tested at a strain rate of $3.0 \times 10^3\ s^{-1}$ and a temperature of 25 °C. It can be seen that the specimen failed along a plane orientated at 45° to the loading direction. This plane corresponds to the plane of maximum shear stress, and thus it is inferred that the specimen fractured as the result of localised shearing. Fig. 5a and b present SEM fractographs of two Ti–6Al–4V specimens deformed at a temperature of −150 °C and strain rates of $1.0 \times 10^3\ s^{-1}$ and $4.3 \times 10^3\ s^{-1}$, respectively. The dimple-like features on the two fracture surfaces indicate that the dominant fracture mechanism is one of transgranular ductile failure. Furthermore, comparing the two fracture surfaces, it is observed that the dimple density increases with an increasing strain rate. Similar tendencies are noted in Fig. 5c, d and e, f at temperatures of 0 °C and 25 °C, respectively. Comparing the three sets of figures, it is found that the dimple density reduces and the number of flat cleavage planes increases as the temperature reduces. In other words, the ductility of the Ti–6Al–4V alloy reduces as the deformation temperature is reduced. This result is consistent with the stress–strain curves presented in Fig. 2a–c, which show that the fracture strain increases with an increasing strain rate or an increasing temperature.

3.4. Microstructural observations and analysis

Fig. 6 presents a TEM image of an undeformed Ti–6Al–4V specimen at a temperature of 25 °C. It is observed that the microstructure contains a small number of dislocations and has a stacking fault arrangement. Fig. 7a–f shows the dislocation structures of Ti–6Al–4V specimens deformed at temperatures of −150 °C, 0 °C

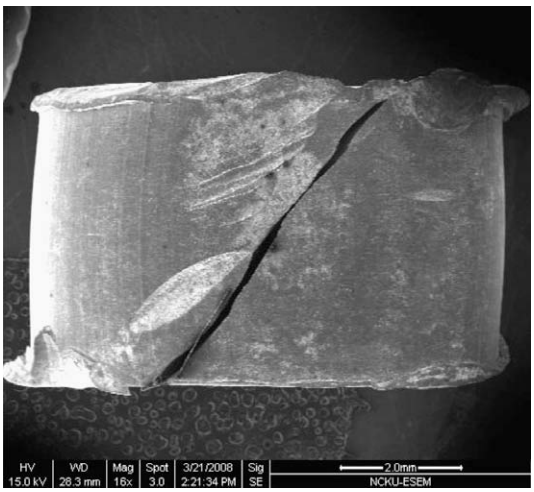

Fig. 4. Low-magnification SEM fractograph of Ti–6Al–4V specimen deformed at strain rate of $3.0 \times 10^3\ s^{-1}$ and temperature of 25 °C.

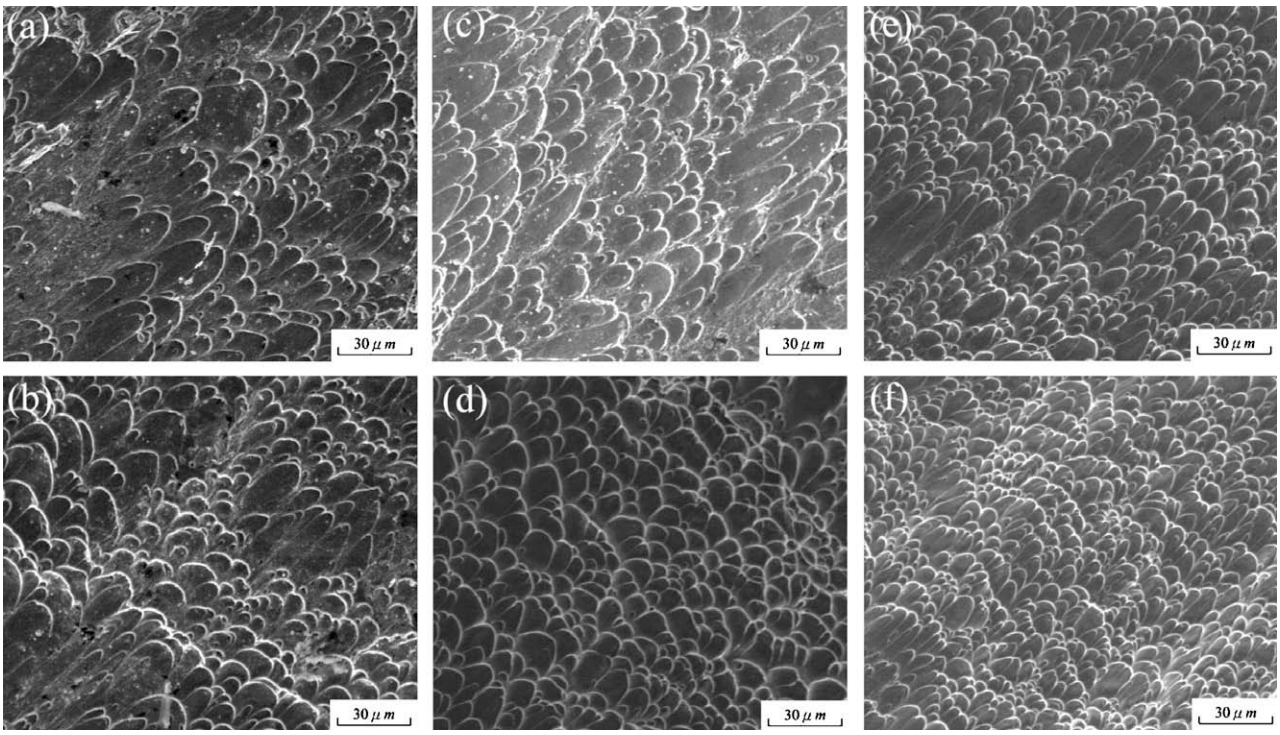

Fig. 5. Fracture surfaces of Ti–6Al–4V specimens deformed at: (a) −150 °C, 1.0×10^3 s^{-1}; (b) −150 °C, 4.3×10^3 s^{-1}; (c) 0 °C, 1.0×10^3 s^{-1}; (d) 0 °C, 4.3×10^3 s^{-1}; (e) 25 °C, 1.0×10^3 s^{-1}, and (f) 25 °C, 4.3×10^3 s^{-1}.

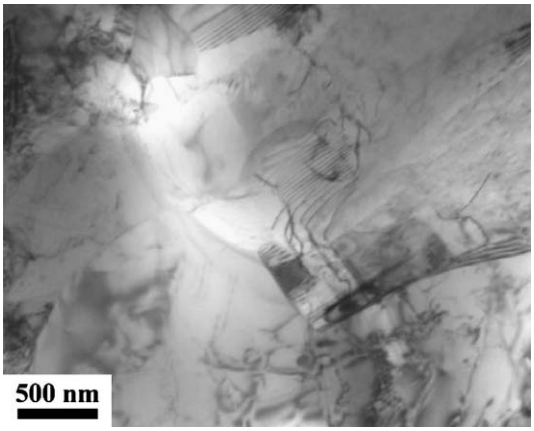

Fig. 6. TEM micrograph of undeformed Ti–6Al–4V specimen at temperature of 25 °C.

and 25 °C under strain rates of 1.0×10^3 s^{-1} and 4.3×10^3 s^{-1}, respectively. In every case, it can be seen that the deformed microstructure contains dislocation cells. It is thought that the presence of these dislocation structures is the result of the high stacking fault energy of Ti–6Al–4V alloy [34]. Comparing Fig. 7a and b, it is observed that at a very low temperature of −150 °C, the number of dislocations increases and the average size of the dislocation cells decreases as the strain rate is increased. The increased dislocation density prompts the formation of a tangled dislocation structure, which reduces the mobility of the dislocations and therefore enhances the resistance of the Ti–6Al–4V alloy to plastic deformation. Thus, as shown in the stress–strain curves in Fig. 2a–c, for a constant true strain and a temperature of −150 °C, the flow stress increases with an increasing strain rate. A similar strain-rate dependency is also observed in the specimens deformed at temperatures of 0 °C and 25 °C, respectively. However, comparing the microstructures of the specimens deformed at a constant strain rate (e.g. 1.0×10^3 s^{-1}) but at an increasing temperature (Fig. 7a, c and e), it is seen that a gradual annihilation of the dislocations takes place as the deformation temperature is increased. Thus, while the microstructure of the specimen deformed at a temperature of 25 °C still contains dislocation cells, the average cell size is larger than that in the specimens tested at −150 °C or 0 °C, respectively. The larger size cell provides a wider free path for the mobile dislocations, and therefore results in a softening effect. Hence, a reduction in the work hardening rate and material strength occurs (see Table 2 and Fig. 2a–c).

In this study, the correlation between the microstructural evolution of Ti–6Al–4V alloy and its macroscopic behaviour was evaluated quantitatively under various strain rate and temperature conditions by computing the dislocation density within the various fracture specimens using the method proposed by Ham [35], i.e. $\rho = 2n/Lt$, where n is the number of intersections between a particular dislocation and a random set of lines of length L and t is the foil thickness. The values of n, L and t were determined by drawing five lines with a total length of L in random directions on TEM images with a magnification of 100,000×, and then counting the total number of dislocations intersecting these lines in order to obtain the value of n. Finally, the foil thickness, t, was measured using a convergent beam diffraction technique.

Table 3 summarises the dislocation density and cell size characteristics of Ti–6Al–4V alloy specimens deformed at a true strain of 0.1 under different strain rates and temperatures. It is seen that the dislocation density increases with an increasing strain rate, but decreases with an increasing temperature. Fig. 8 plots the variation of the true stress values given in Fig. 2 against the square root of the dislocation density ($\sqrt{\rho}$), and confirms the presence of a Bailey–Hirsch type relation. Substituting parameter values of $G = 42.5$ GPa [36], $b = 3.0 \times 10^{-10}$ m [33] and $\sigma_0 = 915$ MPa [37] into Eq. (1), the value of α_1 is determined to be $\alpha_1 \cong 0.42$. Table

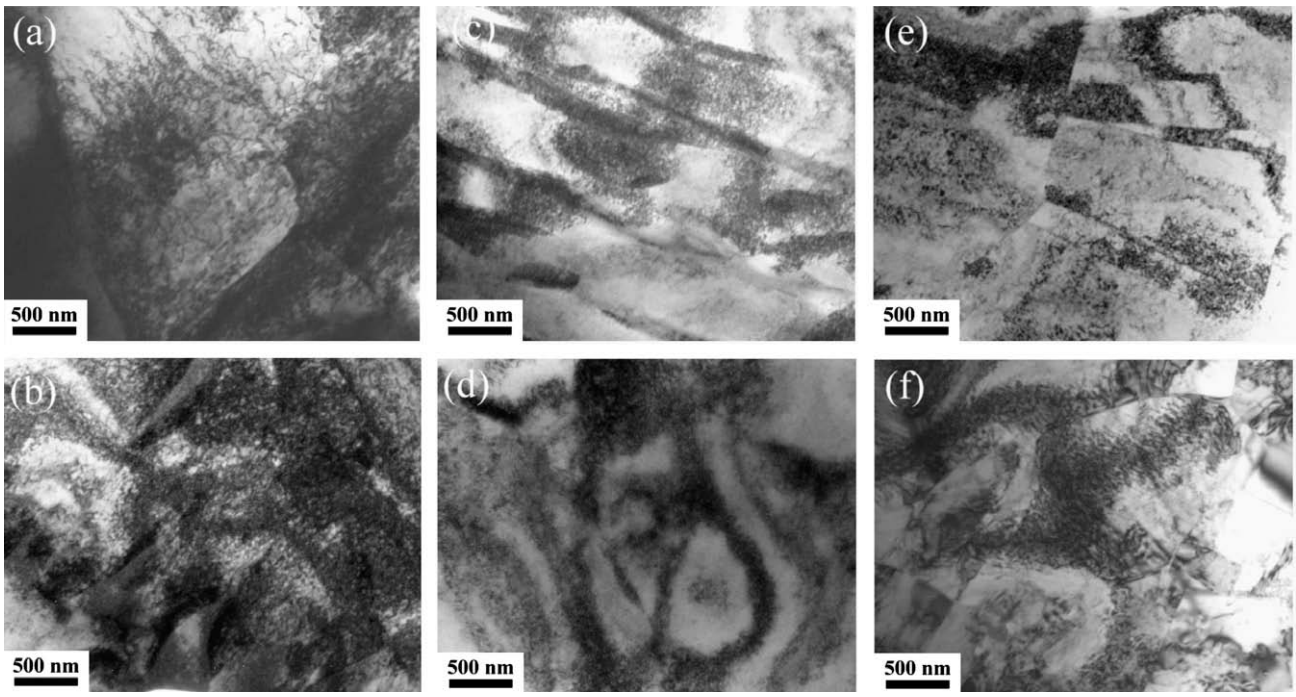

Fig. 7. TEM micrographs of dislocation microstructures of Ti–6Al–4V specimens deformed at: (a) −150 °C, 1.0×10^3 s^{-1}; (b) −150 °C, 4.3×10^3 s^{-1}; (c) 0 °C, 1.0×10^3 s^{-1}; (d) 0 °C, 4.3×10^3 s^{-1}; (e) 25 °C, 1.0×10^3 s^{-1}; and (f) 25 °C, 4.3×10^3 s^{-1}.

Table 3
Dislocation density and cell size of Ti–6Al–4V alloy deformed at true strain of 0.1 under different strain rates and temperatures.

T (°C)	Strain rate (s^{-1})	Stress (MPa)	Dislocation density (10^{10} cm^{-2})	Dislocation cell (μm)
25	1000	1050	11.2	0.56
	3000	1099	14.7	0.51
	4300	1135	17.6	0.50
0	1000	1061	12.5	0.54
	3000	1119	17	0.51
	4300	1157	18.9	0.49
−150	1000	1138	17.7	0.51
	3000	1207	23.2	0.48
	4300	1253	25.6	0.45

3 also shows that the dislocation cell size decreases with increasing strain rate, but increases with increasing temperature. Fig. 9 shows the variation of the true stress with the dislocation cell size. The relationship between the average dislocation cell size, the true stress and the hardening behaviour can be described by [38]

$$\sigma - \sigma_0 = \alpha_2 G \left(\frac{b}{d}\right)^m \tag{4}$$

where d is the average dislocation cell size, σ_0 is the initial yield stress, G and b are the shear modulus and Burgers vector, respectively, and α_2 and m are constants. In general, the value of $-m$ (minus m) shows the power of the dislocation cell walls, or the effect of the dislocation cell size on the flow stress. Utilising the values presented in Table 3 for the stress and dislocation cell size, α_2 and m are found to have values of $\alpha_2 = 1.73 \times 10^9$ and $m = 3.57$.

Microscopically, the grain boundaries of polycrystalline materials act as barriers to dislocation motion. For general engineering materials, the strength is related to the grain size via the following Hall–Petch relationship [39]:

$$\sigma = \sigma_0 + kd^{-\frac{1}{2}}, \tag{5}$$

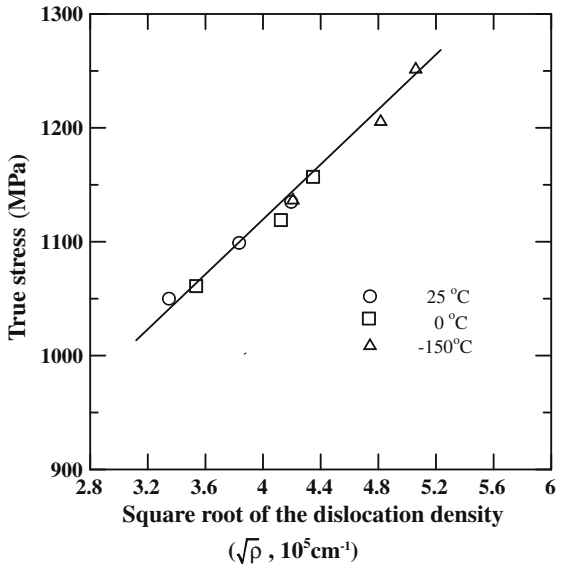

Fig. 8. Variation of flow stress with square root of dislocation density for Ti–6Al–4V alloy deformed at constant true strain of 0.1.

where σ_0 and k are constants and d is the mean grain size. This relationship clearly shows that the strength of the material is related to the grain size by a power of −1/2.

It has been reported that stacking-fault free energy effects have a significant impact on deformed microstructures [40]. In high stacking-fault free energy materials, partial dislocations are not appreciably extended and cross-slip is favoured. Extensive cross-slip gives rise to dislocation cell structures which form a minimum energy configuration as the dislocation density increases in response to large deformations and high strain rates. Typically, dislocation cell structures are formed in impact loaded metals when

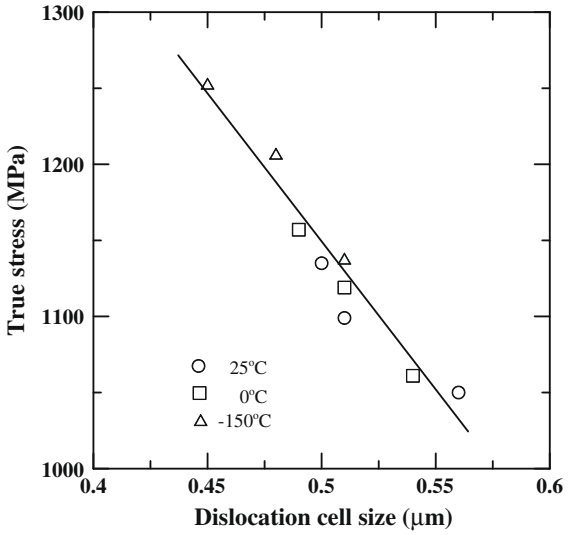

Fig. 9. Variation of flow stress with dislocation cell size for Ti–6Al–4V alloy deformed at constant true strain of 0.1.

the stacking-fault free energy exceeds a value of approximately 60 mJ/m^2.

Since titanium alloy has a high stacking-fault free energy (i.e. 110 mJ/m^2 [41]), the appearance of cell structures within the present deformed specimens is not unexpected. These cells impose a grain refinement effect upon the undeformed material, and the resulting change in the flow stress with increasing strain rate is given by Eq. (4) with $m = 3.57$. This value of m is approximately seven times greater than that of the power term in Eq. (5), and is also notably higher than that of other materials deformed under low strain rates at room temperature or elevated temperature conditions [42]. For example, $m = 1$ for polycrystalline aluminum deformed at 20 °C and 4×10^{-3} s^{-1} [43], $m = 1.06$ for Ni-20–Cr–2ThO$_2$ alloy deformed to a plastic strain of 0.15 at 700, 900 and 1100 °C, respectively, and cross-head speeds of 5.08×10^{-3} mm/min or 5.08×10^{-1} mm/min [44], and $m = 0.98$ for Al–Zn alloy in double shear and creep tests performed at strain rates ranging from 1.6×10^{-6} to 2×10^{-3} s^{-1} and temperatures of 650–893 K [45]. Thus, it is inferred that the large value of m observed in the present impacted specimens is the result of the dislocation cell structure induced by a cryogenic deformation temperature and a high strain rate.

4. Conclusions

This study has conducted an experimental investigation into the effects of the strain rate on the impact response and microstructural evolution of Ti–6Al–4V alloy at strain rates ranging from 1.0×10^3 s^{-1} to 4.3×10^3 s^{-1} and temperatures in the range of −150 °C to 25 °C. The experimental results have shown that the flow stress, yield strength and work hardening coefficient all increase with increasing strain rate, but decrease with increasing temperature. Moreover, as the strain rate is increased, the strain rate sensitivity increases, but the activation volume decreases. The SEM observations have shown that the fracture surfaces are characterised by a transgranular dimple structure, which indicates that the Ti–6Al–4V specimens fail in a ductile mode. The fracture strain increases with an increasing dimple density. The TEM observations have shown that the dislocation density increases with an increasing strain rate, but decreases with an increasing temperature. The flow stress induced within the Ti–6Al–4V specimens varies with the square root of the dislocation density under the current test conditions. In other words, the flow stress response of the Ti–6Al–4V specimens conforms to a Bailey–Hirsch type relation. Finally, the results have shown that the size of the dislocation cells has a greater strengthening effect on the flow stress than the grain boundaries.

Acknowledgements

The authors gratefully acknowledge the financial support provided to this study by the National Science Council (NSC) of Taiwan under Contract No. NSC 96-2221-E-006-048.

References

[1] R.A. Wood, Titanium Alloy Handbook, Metals and Ceramics Information Center Battelle, Publication No. MCIC-HB-02, December 1972.
[2] I. Gurrappa, Mater. Charact. 51 (2003) 131–139.
[3] M. Yamada, Mater. Sci. Eng. A 213 (1996) 8–15.
[4] N.P. Laverov, A.A. Sarkisov, Herald Russ. Acad. Sci. 7614 (2006) 399–406.
[5] A. Baskaran, An assessment of nuclear and missile developments in South Asia, in: 7th Annual Conference on Economic and Security, Burwalls Hall, Bristol University, Bristol, 26–28 June 2003.
[6] J.S. Bermudez, A History of Ballistic Missile Development in the DPRK, Occasional Paper No. 2, Center for Nonproliferation Studies, Monterey Institute of International Studies, Monterey CA, 1999
[7] W.S. Lee, T.J. Liu, J. Nucl. Mater. 359 (2006) 247–257.
[8] W.S. Lee, C.Y. Lin, C.Y. Liu, F.T. Tzeng, J. Nucl. Mater. 335 (2004) 335–344.
[9] Q. Li, Y.B. Xu, M.N. Bassim, J. Mater. Process. Technol. 155–156 (2004) 1889–1892.
[10] Q. Xue, X.Z. Liao, Y.T. Zhu, G.T. Gray, Mater. Sci. Eng. A 410–411 (2005) 252–256.
[11] A.G. Odeshi, G.M. Owolabi, M.N.K. Singh, M.N. Bassim, Metall. Mater. Trans. A 38A (2007) 2674–2680.
[12] W.S. Lee, T.H. Chen, H.H. Hwang, Metall. Mater. Trans. A 39A (2008) 1435–1448.
[13] W.S. Lee, T.H. Chen, Scripta Mater. 54 (2006) 1463–1468.
[14] S.P. Timothy, Acta Metall. 35 (1987) 301–336.
[15] R. Nakkalil, J.R. Hornaday Jr., M.N. Bassim, Mater. Sci. Eng. A141 (1991) 247–260.
[16] A.G. Odeshi, S. Al-ameeri, M.N. Bassim, J. Mater. Process. Technol. 162–163 (2005) 385–391.
[17] W.S. Lee, C.Y. Liu, T.H. Chen, J. Nucl. Mater. 374 (2008) 313–319.
[18] A. Uenishi, C. Teodosiu, E.V. Nesterova, Mater. Sci. Eng. A 400–401 (2005) 499–503.
[19] W.S. Lee, T.H. Chen, Mater. Chem. Phys. 113 (2009) 734–745.
[20] X. Feaugas, Acta Mater. 47 (1999) 3617–3632.
[21] K. Yasunaga, M. Iseki, M. Kiritani, Mater. Sci Eng. A 350 (2003) 76–80.
[22] M.E. Kassner, Acta Mater. 52 (2004) 1–9.
[23] H. Jarmakani, J.M. McNaney, B. Kad, D. Orlikowski, J.H. Nguyen, M.A. Meyers, Mater. Sci. Eng. A 463 (2007) 249–262.
[24] Y. Tomota, P. Lukas, S. Harjo, J.H. Park, N. Tsuchida, D. Neov, Acta Mater. 51 (2003) 819–830.
[25] W.S. Lee, C.F. Lin, J. Mater. Process. Technol. 75 (1998) 127–136.
[26] S.V. Kailas, Y.V.R.K. Prasad, S.K. Biswas, Metall. Mater. Trans. A 25A (1994) 2173–2179.
[27] M. Mier, A.K. Mukherjee, Scripta Metall. Mater. 24 (1990) 331–336.
[28] W.S. Lee, C.F. Lin, Mater. Sci. Eng. A 241 (1998) 48–59.
[29] W.S. Lee, T.H. Chen, Mater. Trans. 47 (2006) 355–363.
[30] P. Ludwik, Elementte der Technologischen Mechanik, Springer Verlag, Berlin, 1909. p. 32.
[31] S.S. Egg, Y.Q. Sue, P.B. Hirsch, Mater. Sci. Eng. A 308 (2001) (1995) 124–135.
[32] G.B. Gibbs, Mater. Sci. Eng. 4 (1965) 313–328.
[33] J. Warren, L.M. Hisung, H.N.G. Wadley, Acta Metall. Mater. 43 (1995) 2773–2787.
[34] R.E. Reed-Hill, R. Abbaschian, Physical Metallurgy Principles, PWS Publishing Company, 1991. pp. 103–108.
[35] R.K. Ham, Phil. Mag. 6 (1961) 1183–1184.
[36] A.S. Bonnet-Lebouvier, J.R. Klepaczko, Int. J. Impact Eng. 27 (2002) 755–769.
[37] J.O. Peters, R.O. Ritchie, Mater. Sci. Eng. A 319–321 (2001) 597–601.
[38] P. Trivedi, D.P. Dield, H. Weiland, Int. J. Plast. 20 (2004) 459–476.
[39] H. Conrad, Metall. Mater. Trans. A 35A (2004) 2681–2695.
[40] L.E. Murr, Residual microstructure-mechanical property relationships in shock-loaded metals and alloys, in: M.A. Meyers, L.E. Murr (Eds.), Shock Waves and High-strain-rate Phenomena in Metals, Plenum, New York, 1981, pp. 607–613.
[41] C. Woodward, J.M. MacLaren, S. Rao, J. Mater. Res. 7 (1992) 1735–1750.
[42] S.V. Raj, G.M. Pharr, Mater. Sci. Eng. 81 (1986) 217–237.
[43] E.S. Kayali, A. Plumtree, Metall. Trans. A 13A (1982) 1033–1041.
[44] J.H. Hausselt, W.D. Nix, Acta. Metall. 25 (1977) 595–607.
[45] A. Goel, T.T. Ginter, F.A. Mohamed, Effect of stress reductions on the stress exponent and subgrain size in an Al–Zn alloy, Metall. Trans. A 14A (1983) 2309–2318.